Influence of numerical resolution on the dynamics of finite-size particles with the lattice Boltzmann method

Influence of numerical resolution on the dynamics of finite-size particles with the lattice Boltzmann method

C. Livi, G. Di Staso, H. J. H. Clercx, and F. Toschi
Fluids and Flows Group and J.M. Burgers Centre for Fluid Dynamics, Department of Applied Physics, Eindhoven University of Technology, Eindhoven, The Netherlands

(Received 14 July 2020; revised 14 November 2020; accepted 17 December 2020; published 8 January 2021)

We investigate and compare the accuracy and efficiency of different numerical approaches to model the dynamics of finite-size particles using the lattice Boltzmann method (LBM). This includes the standard bounce-back (BB) and the equilibrium interpolation (EI) schemes. To accurately compare the different implementations, we first introduce a boundary condition to approximate the flow properties of an unbounded fluid in a finite simulation domain, taking into account the perturbation induced by a moving particle. We show that this boundary treatment is efficient in suppressing detrimental effects on the dynamics of spherical and ellipsoidal particles arising from the finite size of the simulation domain. We then investigate the performances of the BB and EI schemes in modeling the dynamics of a spherical particle settling under Stokes conditions, which can now be reproduced with great accuracy thanks to the treatment of the exterior boundary. We find that the EI scheme outperforms the BB scheme in providing a better accuracy scaling with respect to the resolution of the settling particle, while suppressing finite-size effects due to the particle discretization on the lattice grid. Additionally, in order to further increase the capability of the algorithm in modeling particles of sizes comparable to the lattice spacing, we propose an improvement to the EI scheme, the *complete equilibrium interpolation* (CEI). This approach allows us to accurately capture the boundaries of the particle also when located between two fluid nodes. We evaluate the CEI performance in solving the dynamics of an under-resolved particle under analogous Stokes conditions and also for the case of a rotating ellipsoid in a shear flow. Finally, we show that EI and CEI are able to recover the correct flow solutions also at small, but finite, Reynolds number. Adopting the CEI scheme it is not only possible to detect particles with zero lattice occupation, but also to increase up to one order of magnitude the accuracy of the dynamics of particles with a size comparable to the lattice spacing with respect to the BB and the EI schemes.

DOI: 10.1103/PhysRevE.103.013303

I. INTRODUCTION

Particle and droplet transport phenomena in complex flows are crucial for many environmental, industrial, and medical applications. Examples include droplets, aerosol, and particle transport in turbulent flows [1,2], but also in red blood cells flow in plasma [3] or contamination from particle debris in next generation lithography machines [4]. This topic is nowadays also extremely relevant in relation with the COVID-19 pandemic [5,6].

To cope with such a wide spectrum of applications, an increasingly growing effort from the scientific community is devoted towards the development of accurate and efficient numerical methods.

Over the past decades, the lattice Boltzmann method (LBM) [7,8] emerged as an efficient and reliable tool to address a large variety of flows, including particle-laden ones [9]. Examples of few outstanding applications of the LBM are simulations of arterial flows [10,11], simulations of finite-size particle dynamics at low Reynolds number [12,13] and in particle-laden turbulent flows [14–16], as well as investigation of particle transport in microchannels [17,18], just to cite some.

According to the original works by Ladd [19,20] and by Aidun [21], solid particles (and nondeformable droplets) can be modeled as finite volumes enclosed by moving boundaries suspended in the fluid domain. Fluid-solid interactions are addressed via no-slip boundary conditions applied at the particle surface. Momentum exchange between the fluid and solid lattice nodes at the interface is used to compute the force and the torque exerted on the solid particle. Newton's equation of motion for the particle can then be directly integrated to update the particle position and velocity.

While this method has been successfully applied to simulate many particle-laden flows, its principal drawback lies in the introduction of discretization effects from the particle representation on the lattice grid. This imposes an approximation of the exact location of the surface of the particle, which is commonly found in between the fluid and solid nodes. In the most common approach, when a standard bounce-back (BB) no-slip rule is applied at the interface, the particle is approximated by a "rough" staircase shape (as sketched by the blue solid line in Fig. 1) leading to a reconstruction of the hydrodynamics around the particle that is, in general, only first-order accurate [22].

Several studies can be found in the literature offering various improvements for the particle discretization. Bouzidi *et al.* [23], Lallemand *et al.* [24], and Ginzburg *et al.* [25] propose different techniques to treat curved and moving

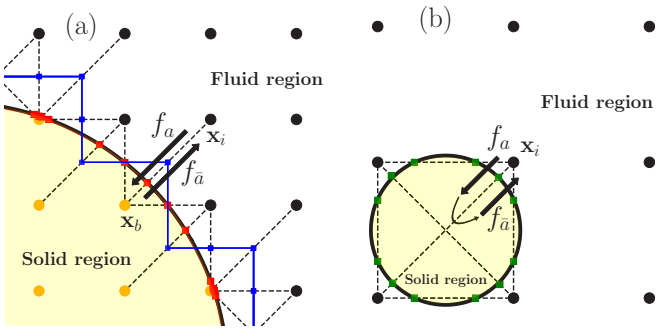

FIG. 1. Sketches of two particles at different resolution on the lattice grid. On the left (a) a particle with radius 2.5 lattice units is represented: momentum exchange is calculated for every fluid node ($\mathbf{x}_i$) and its adjacent solid nodes ($\mathbf{x}_b$) along the fluid-solid links (black dashed lines). The inward component along the direction a of the velocity distribution function f interacts with the surface of the particle during the streaming from $\mathbf{x}_i$ to $\mathbf{x}_b$ and the outward component in the direction $\bar{a}$ is generated. Using standard BB, the interaction point is approximated in the middle position of the fluid-solid link (blue squares), while using an interpolation method the surface of the particle is evaluated in its exact location (red squares). If the particle resolution drops, as shown on the right sketch (b), there might be no lattice nodes enclosed by the solid volume and both BB and EI schemes fail to detect the particle. Using complete equilibrium interpolation it is now possible to detect the particle position and surface (green squares) also between adjacent fluid node links.

boundaries based on second-order accurate interpolation schemes. While improving accuracy of the BB rule and conserving stability, all these methods require additional fluid nodes along the fluid-solid link in order to successfully apply interpolation. Chun *et al.* [22] consider interpolation of the equilibrium distribution only, keeping the second-order accuracy without the need of extra fluid nodes along the fluid-solid links. Kao *et al.* [26] proposed an interpolation-free treatment of the fluid-boundary interaction based on local grid refinement. This approach allows us to improve accuracy while reducing effects of mass fluctuations typical of interpolated schemes related to the reconstruction of the velocity distribution function, at the price of increased complexity and computational load.

On-grid particle description is not the only approach to describe particle transport in the LBM. Wu and Aidun [27] enforced a no-slip boundary condition on the external surface of the solid particle based on the external boundary force (EBF) approach developed by Goldstein *et al.* [28]. The EBF method consists of the application of a force density to the fluid domain to force the difference between the fluid and the solid velocity at the boundary nodes to be zero, resulting in smoother fluid-solid interactions with respect to the standard BB.

Niu *et al.* [29] investigated the possibility to implement a momentum exchange-based method by using two unrelated meshes using the immersed boundary method (IBM) first proposed by Peskin [30], without however increasing the accuracy with respect to standard approaches. A comprehensive comparison between interpolation and IBM is addressed by Peng *et al.* in [31], where it is found that while interpolated schemes are in general more accurate, IBM efficiently suppresses force and torque fluctuations on the particle due to the different representation of the particle surface on the lattice grid. For the scope of this work, we use an on-grid description to investigate and compare the accuracy provided by different fluid-solid interaction models.

The problem of accuracy scaling of on-grid particle description with respect to different resolutions, in the case of nonmoving particles, has been addressed by several authors. For example, Chun *et al.* [22] performed a convergence analysis of the permeability for flows across different arrays of spheres and cubes, while Sanjeevi *et al.* [32] show the scaling of the drag coefficient of a fixed sphere for different resolutions.

When particle motion is taken into account, accuracy can be negatively affected by different mechanisms, such as volume fluctuations and lack of strict mass conservation, induced for example by the reconstruction the distributions at the uncovered fluid nodes, as shown in [24]. These detrimental effects can in principle lead to different convergence rates as a function of particle resolution with respect to the case of stationary particles, especially if the two-way coupling between particle and flow is relevant like in the settling of a particle in the Stokes flow regime. However, fine accuracy measurements in cases where particles are moving coupled with the flow are challenging due to the difficulties related to finding an appropriate benchmark capable of taking into account finite-domain effects. Indeed, in most of the cases where an analytical expression of the motion of the particle is available, the deviations induced by the finite simulation domain are often larger than the one induced by finite-resolution effects related to particle discretization (as shown later in Fig. 4 in Sec. III).

In this work we first address the possibility to reduce the effects of a finite-size domain by focusing on cases where the flow is strongly coupled with the particle motion, namely the settling of a spherical particle in a quiescent fluid and the rotation of spherical particles in a shear flow, both under low-Reynolds number conditions (approaching Stokes flow regime). For these cases we have access to analytical expressions for the flow field in an unbounded domain.

In order to recover these flows under ideal conditions, we propose an adaptive boundary treatment at the boundaries of the simulation domain that allows us to mimic the behavior of an unbounded fluid, allowing us to strongly reduce nonideal effects induced by the finite size of the simulation domain. Accuracy scaling with varying particle resolution can then be finely evaluated for different fluid-solid treatments, namely the standard BB, and the equilibrium-interpolated (EI) bounce-back scheme proposed by Chun *et al.* [22].

We introduce an improvement of the aforementioned EI scheme that allows us to detect very small particles in the framework of the standard momentum-exchange interaction scheme. This method will be addressed as *complete equilibrium interpolation* (CEI) and it will be compared with the aforementioned EI scheme in cases where the simulated particles are described by very few lattice nodes. As an addition to the investigation under Stokes flow conditions presented in this work, we show in Appendix A that for fully resolved particles EI and CEI recover the expected flow behavior also in cases where the Reynolds number is small, but finite.

The final motivation of this work is the understanding and fine measurements of the accuracy scaling of momentum-exchange methods with respect to particle resolution, with a focus on cases when their computational resolution is decreased to just a few grid points. The possibility to efficiently simulate smaller particles without a loss in accuracy when compared to standard approaches can be a valuable tool for simulations of dense suspensions, where many more particles can now be simulated without loss in accuracy and without up-scaling the simulation size to larger resolutions, greatly increasing the computational efficiency. The feature to be sensible to surface details as small as the lattice spacing can be relevant also for fully resolved particles with complex shape or fine surface details; these details can now be captured with more precision.

The paper is structured as follows: in Sec. II the numerical method is presented as well as the details of the moving-boundary algorithm. In Sec. III the problem of reproducing ideal Stokes flow for the settling of a spherical particle is addressed and results related to particle resolution analysis for different fluid-solid interaction models are presented. We investigate the performances for the same interaction models in resolving the angular dynamics of an ellipsoid in a shear flow at low Reynolds number in Sec. IV. We summarize and discuss our results in Sec. V.

II. NUMERICAL METHOD

A. Regularized lattice Boltzmann method

In this work we adopt a standard D3Q19-BGK and a D3Q27-BGK lattice-Boltzmann method featuring a projection-based regularization (PR) [33] for the precollision velocity distribution function (VDF) f, based on Hermite polynomial expansion. In few words, the PR-LBM solves the discretized Boltzmann equation for the discrete VDFs, for a set of discrete lattice velocities $\mathbf{e}_a$ with $a = 0, \ldots, d-1$ where d is the lattice velocity number, at position $\mathbf{x}$ and time t given by

$$f_a(\mathbf{x} + \mathbf{e}_a t, t + \Delta t) = f_a^{(0)}(\mathbf{x}, t) + \left(1 - \frac{1}{\tau}\right)\hat{f}_a'(\mathbf{x}, t) + F_a, \tag{1}$$

where $f_a^{(0)}(\mathbf{x}, t)$ are the equilibrium VDFs, $\hat{f}_a'$ are the regularized precollisions VDFs, F_a represents an external body force, and the relaxation time τ is directly related to the fluid viscosity by $\nu = c_s^2(\tau - 1/2)$, with c_s^2 the speed of sound ($c_s^2 = 1/3$ for D3Q19 and D3Q27). In this work we use standard lattice units, so that $\Delta x = 1$ and $\Delta t = 1$.

The PR procedure has been extensively described in several previous works [33,34], so that here we will provide just the most important features: it consists of filtering out all the nonhydrodynamic contributions from the time evolution in order to stabilize the LBM and, e.g., reduce numerical slip effects at fluid-solid interfaces.

The VDF is split into two components:

$$f_a = f_a' + f_a^{(0)}, \tag{2}$$

where f_a' is the nonequilibrium part of the total distribution. Since $f^{(0)}$ already lies entirely on the subspace spanned by the first N Hermite polynomials, the PR procedure allows us to convert this nonequilibrium part into the new distribution $\hat{f}_a'$ which lies in the same subspace. The components of the VDF thus read

$$f_a^{(0)} = w_a \rho \left[1 + \frac{\mathbf{e}_a \cdot \mathbf{u}}{c_s^2} + \frac{3(\mathbf{e}_a \cdot \mathbf{u})^2 - u^2}{2c_s^2}\right], \tag{3}$$

$$\hat{f}_a' = w_a \sum_{n=0}^{N} \frac{1}{n!} \mathbf{a}^{(n)} \mathcal{H}^{(n)}(\mathbf{e}_a), \quad a = 0, \ldots, d-1, \tag{4}$$

$$\mathbf{a}^{(n)} = \sum_{a=1}^{d} f_a' \mathcal{H}^{(n)}(\mathbf{e}_a), \quad n = 0, \ldots, N, \tag{5}$$

where w_a is the lattice weight relative to direction a, $\mathbf{u}$ and ρ are the macroscopical fluid velocity and density at the lattice node, $\mathcal{H}^{(n)}$ is the nth Hermite polynomial, $\mathbf{a}^{(n)}$ is the corresponding expansion coefficient, and N is the maximum order of expansion provided by the Gauss-Hermite quadrature (see Appendix B for the explicit expressions of $\boldsymbol{e}_a$, w_a, and $\mathcal{H}^{(n)}$). The D3Q19 scheme allows a complete projection up to $N = 2$, such that weakly incompressible, isothermal flows are completely recovered at a Navier-Stokes level of description, meaning that when a no-slip rule is applied on a solid boundary the slip velocity at its surface should be identically zero. Since the first two Hermite coefficients vanish due to the vanishing contribution from the nonequilibrium distributions to mass and momentum, the projection of the nonequilibrium distributions is given by

$$\hat{f}_a' = w_a \frac{\mathcal{H}^{(2)}(\mathbf{e}_a)}{2} \sum_{b=1}^{d} f_b' \mathbf{e}_b \mathbf{e}_b. \tag{6}$$

This method has been applied already to a large variety of flows, including multicomponent flow applications [35] and rarefied gas flows [36], demonstrating its capability to improve the accuracy and stability of standard LBM simulations.

In the context of the present work, we adopt the PR-LBM because of its ability to suppress the residual numerical slip that can appear around the particle in cases where its dimension is small compared to the lattice grid. It has been indeed shown [37] that for a planar Poiseuille channel flow discrete effects related to the nature of the LBM produce a numerical slip at the fluid-wall interfaces. The slip velocity produced on the walls of the channel, using a standard LBM model with BB rule, is

$$U_s = \frac{32}{\pi} Kn^2 - \frac{1}{L^2}, \tag{7}$$

where

$$Kn = \sqrt{\frac{\pi}{2}} c_s \frac{\tau - 0.5}{L} \tag{8}$$

is the Knudsen number and L is a characteristic spatial length of the simulated system. As shown in Fig. 2, using a PR-LBM it is possible to strongly suppress the numerical slip at walls, even if some small slip still appears for large values of Kn. In our simulations the characteristic spatial length L is replaced by the typical size of the particle and while an analytical relation such as Eq. (7) for the numerical slip around the particle

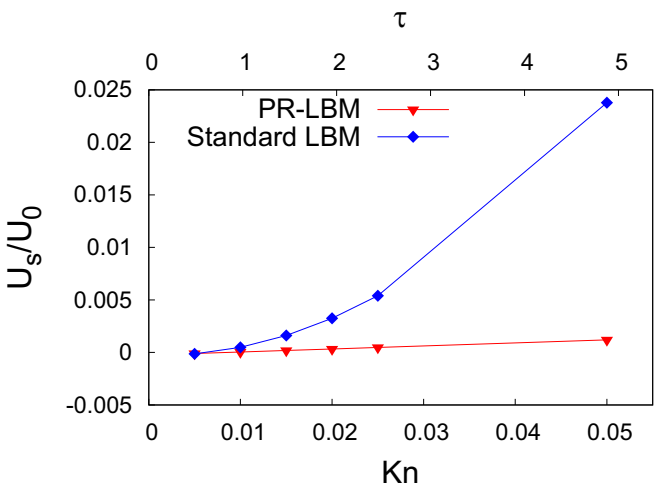

FIG. 2. Comparison of the slip velocity at the walls U_s normalized with respect to the center channel velocity U_0 of a rectangular 2D Poiseuille channel flow for standard LBM (blue diamonds) and for projection-based regularized LBM (PR-LBM, red triangles), as a function of Kn (bottom axis) and τ (top axis), for a fixed channel width $L = 64$. When a strict no-slip boundary condition on the walls is imposed, the slip velocity should be identically zero at any Kn number, but due to the discrete nature of the LBM a numerical slip velocity can appear. A PR-LBM strongly suppresses the numerical slip produced at the channel walls, especially for large values of Kn. Here the walls are located at the middle position between the fluid and the solid nodes, so that BB and EI schemes are equivalent.

is missing for curved boundaries, we expect the PR-LBM to reduce such effects when compared to a standard LBM scheme.

B. Fluid-solid interactions

We model fluid-solid interactions between flow and particles following the algorithm introduced by Aidun *et al.* [21], which combines a Lagrangian description of the solid particle with the LBM solver for the fluid phase. The momentum contribution of a fluid grid point in contact with the solid particle is obtained by the summation of the inward and outward momentum for each fluid-solid link given by

$$\mathbf{p}_a = \mathbf{e}_a[f_a(\mathbf{x}_b, t) + f_{\bar{a}}(\mathbf{x}_i, t)], \tag{9}$$

where we denote with the subscript b a node belonging to the solid, i a fluid node in the vicinity of b, and with a the velocity direction pointing from i to b. The subscript $\bar{a}$ refers to the velocity direction opposite to a, as shown in Fig. 1.

Since the particle is moving across the lattice grid, two extra sources of momentum must be taken into account, namely the momentum gained by the particle when covering new fluid nodes and the momentum lost by the particle when uncovering a (former) solid node [21].

Once the total momentum exchange between the fluid and the solid particle is evaluated, the equations of motion of the particle are integrated through a leapfrog scheme to update its translational and rotational velocity, position, and orientation [19,21].

The outward momentum, i.e., from solid to fluid, given by $f_{\bar{a}}(\mathbf{x}_i, t)$ in Eq. (9), is obtained by enforcing a no-slip rule on the particle surface. Such a condition can be applied through different boundary condition schemes. In this work we focus on an accuracy comparison between the BB rule that leads to a staircase approximation of the surface of the particle, and the EI scheme [22] which allows us to correctly detect the particle surface at its actual position on the fluid-solid link. The EI method consists of applying a BB rule to the nonequilibrium component of the VDF:

$$f'_{\bar{a}}(\mathbf{x}_i, t + \Delta t) = f'_a(\mathbf{x}_i, t), \tag{10}$$

while a linear interpolation is applied to the equilibrium part as follows:

$$f^{(0)}_{\bar{a}}(\mathbf{x}_i, t + \Delta t) = 2q f^{(0)}_a(\mathbf{x}_i, t) + (1 - 2q) f^{(0)}_a(\mathbf{x}_i - \mathbf{e}_a, t), \quad \text{for } 0 \leqslant q < 1/2, \tag{11}$$

$$f^{(0)}_{\bar{a}}(\mathbf{x}_i, t + \Delta t) = \frac{1}{2q} f^{(0)}_a(\mathbf{x}_i, t) + \frac{2q - 1}{2q} f^{(0)}_{\bar{a}}(\mathbf{x}_i, t), \quad \text{for } 1/2 < q \leqslant 1, \tag{12}$$

where q denotes the distance of the fluid node to the solid boundary (nondimensionalized by the grid spacing). In this work the exact value of q is evaluated through the ray-sphere intersection algorithm described in [38].

The effects of moving boundaries on the fluid are taken into account by adding to the right-hand side of Eqs. (11) and (12) an additional term $\delta f_{\bar{a}}$ proportional to the velocity $\mathbf{u}_b$ at boundary node b. Following the scheme proposed by Bouzidi *et al.* [23], first-order contributions from the motion of the boundary are given by

$$\delta f_{\bar{a}} = 2 w_a \mathbf{e}_a \cdot \mathbf{u}_b, \qquad \text{if } q < 1/2, \tag{13}$$

$$\delta f_{\bar{a}} = \frac{1}{q} w_a \mathbf{e}_a \cdot \mathbf{u}_b, \qquad \text{if } q \geqslant 1/2. \tag{14}$$

III. ADAPTIVE BOUNDARY CONDITIONS TO SIMULATE STOKES SETTLING

In this section we present the definition of an adaptive boundary treatment of the computational domain boundaries for the case of a spherical particle settling under the effects of gravity in Stokes conditions. Thanks to this approach we are able to strongly reduce the effects of the finite simulation domain on the dynamics of the moving particle, allowing us to perform precise accuracy measurements.

In the most general case, the form of the velocity and pressure fields at position $\mathbf{x}$ in a reference system centered on a particle moving in an unbounded fluid are given by

$$\mathbf{u}(\mathbf{x}) = \mathbf{u}^\infty + \boldsymbol{\Omega}^\infty \times \mathbf{x} + \mathbf{E}^\infty \cdot \mathbf{x} + \mathbf{u}', \tag{15}$$

$$p = p^\infty + p', \tag{16}$$

where $\mathbf{u}^\infty$ and p^∞ are the fluid velocity and pressure at infinity (i.e., far from the particle), $\boldsymbol{\Omega}^\infty$ and $\mathbf{E}^\infty$ are the ambient vorticity and strain, and the primed quantities represent the

perturbation induced by the presence of the moving particle, which can be decomposed into

$$\mathbf{u}' = \mathbf{u}'_t + \mathbf{u}'_r + \mathbf{u}'_s, \tag{17}$$

$$p' = p'_t + p'_s, \tag{18}$$

where the subscripts t, r, and s are abbreviations for *translation, rotation*, and *strain*, respectively. It has to be noted that the rotational term in Eq. (16) is zero, as rotational motion does not influence the pressure field.

In the case of a spherical particle moving at velocity $\mathbf{U}_P$ and rotating at angular velocity $\boldsymbol{\omega}_P$, the analytical expressions for the perturbations in Eqs. (17) and (18) are available [39], and read as

$$u'_{t,i} = \frac{3R}{4} U_{P,j}\left(\frac{\delta_{ij}}{r} + \frac{x_i x_j}{r^3}\right) + \frac{3R^3}{4} U_{P,j}\left(\frac{\delta_{ij}}{3r^3} + \frac{x_i x_j}{r^5}\right), \tag{19}$$

$$u'_{r,i} = \left(\frac{R}{r}\right)^3 \varepsilon_{ijk}(\omega_{P,j} - \Omega^{\infty}_j)x_k, \tag{20}$$

$$u'_{s,i} = -\frac{5R^3}{2}\frac{x_i(x_j E_{\infty,jk} x_k)}{r^5} - \frac{R^5}{2} E_{\infty,jk}\left[\frac{\delta_{ij}x_k + \delta_{ik}x_j}{r^5} - \frac{5x_i x_j x_k}{r^7}\right], \tag{21}$$

where u'_i is the component i of the fluid velocity at position $\mathbf{x}$ in the reference system centered on the particle, R is the particle radius, and r is the distance between $\mathbf{x}$ and the particle center.

Analogously for the pressure the analytical solutions read

$$p'_t = \frac{3\mu R}{2}\frac{U_{P,j}x_j}{r^3}, \tag{22}$$

$$p'_s = -5\mu R^3 \frac{x_i E_{\infty,ij} x_j}{r^5}, \tag{23}$$

where μ is the dynamic viscosity of the fluid.

In this section we address the problem of the settling of a spherical particle under the effect of gravity in an otherwise unperturbed fluid, so that all the external ambient fields are set to zero and the perturbations induced by the particle reduce to Eqs. (19) and (22).

When the particle motion is caused by an external acceleration $\boldsymbol{g}$, e.g., gravity, the final settling velocity $\boldsymbol{U}_0$ is given by the well-known relation

$$\boldsymbol{U}_0 = \frac{2(\rho_p - \rho_f)\boldsymbol{g}R^2}{9\mu}, \tag{24}$$

where ρ_f and ρ_p are the fluid and the particle density, respectively. In the rest of the paper we will address only motion along the $-z$ direction, so that $\boldsymbol{g} = (0, 0, -g)$, $\boldsymbol{U}_P = (0, 0, U_P)$, and $\boldsymbol{U}_0 = (0, 0, U_0)$.

Simulating the settling of a particle in the ideal Stokes regime (which formally requires an unbounded domain) is not possible using standard boundary conditions (e.g., no-slip or periodic) on the domain boundaries of the simulation box. In these kinds of simulations of the dynamics of finite-volume particles, in fact, two main sources of errors are typically present: one is introduced by the finite size of the simulation domain, and another comes from resolution effects due to the discretization of the particle. The influence of domain boundaries on the overall accuracy of the Stokes flow description is significant, making it unfeasible to use the Stokes settling problem and the computation of the terminal settling velocity as an accuracy estimator for the numerical scheme. To overcome such limitations we propose a method to mimic unbounded fluid within a finite simulation domain by exploiting the analytical solution for the Stokes flow problem under investigation.

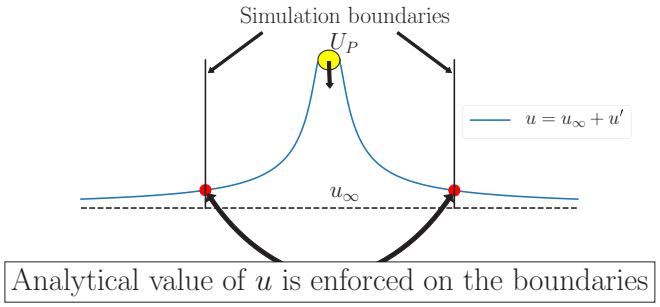

FIG. 3. Sketch of the application of the adaptive boundary condition for the problem of a settling sphere. The analytical value of the velocity field (and of the pressure field) produced by a spherical particle settling at velocity $\boldsymbol{U}_P$ is enforced on the boundary nodes in order to emulate the properties of an unbounded fluid. At infinite distance from the particle the flow velocity is the unperturbed one, defined with u_∞.

The dynamics of the particle and the fluid inside the computational domain are fully resolved using the PR-LBM, while we impose on the boundary nodes (see sketch in Fig. 3) the macroscopic velocity $\mathbf{u}$ and the pressure p according to Eqs. (15) and (16), where the instantaneous particle velocity U_P (as computed from the simulation) and its radius R are used to calculate the analytical values. In the LBM framework this is done by setting the equilibrium distribution $f^{(0)}$ given in Eq. (3) on the boundary nodes.

In this way, even if the particle velocity is affected by an error related to the particle discretization, we are able to reproduce the Stokes velocity field of a sphere moving with speed U_P, largely reducing the impact of having a finite-size simulation box. An example of the improvement is shown in Fig. 4, where the particle velocity is plotted for different boundary conditions and sizes of the computational domain. While in the case of periodic boundary conditions the particle would indefinitely accelerate due to the interactions with its mirror images, imposing no-slip at the domain boundaries would lead to a severe underestimate of the Stokes terminal velocity also for very large sizes of the simulation domain. As a proof of concept of the method, we apply the same approach to a more complex case, i.e., the settling of two vertically aligned identical spheres. The analytical solution for this case can be obtained from Lamb's general expression of the velocity perturbations generated by two moving spheres, as from [40]. While the general solution by Lamb consists of an infinite series of terms from a spherical harmonic expansion, for the sake of simplicity we only impose on the domain boundaries its truncation to the first order. Notwithstanding this

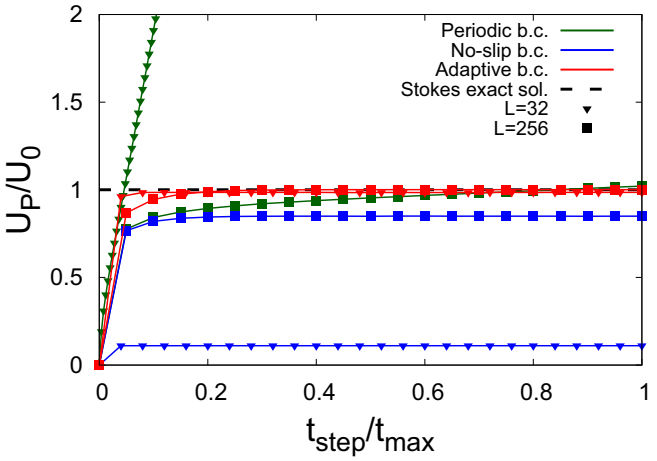

FIG. 4. Particle velocity $\boldsymbol{U}_P$ normalized with the Stokes velocity U_0, defined in Eq. (24), is plotted for no-slip (blue), periodic (green), and adaptive (red) boundary conditions applied on the simulation box of different sizes L with respect to a fixed particle radius R. The ideal Stokes settling velocity is recovered only using an adaptive domain boundary that mimics the behavior of an unbounded fluid. Results here represented correspond to $R = 10$, $\tau = 0.85$, $\rho_p = 2\rho_f$, and $Re = 10^{-3}$.

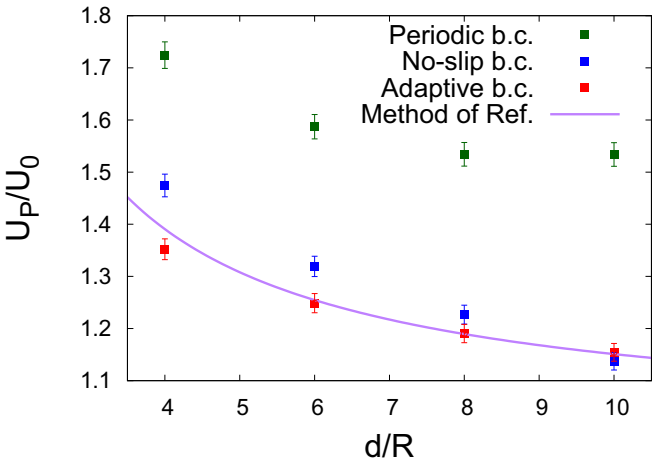

FIG. 5. Terminal velocity U_P, averaged over the last 100 time steps, of two vertically aligned spheres settling under gravity as a function of the distance between the centers of the spheres d over their radius R. The simulation domain size is fixed to $L = 180$, while $\tau = 0.6$ and $\rho_p = 2\rho_f$. Results using the adaptive treatment on the simulation domain boundaries (red squares) are compared with the ones obtained using periodic (green squares) and no-slip (blue squares) conditions. For the adaptive case, the general solution from Lamb, truncated to the first term, is applied on the domain boundaries to simulate Stokes settling of two vertically aligned spheres. Results are in fairly good agreement with the predictions from the method of reflections, computed at first reflection, from Eq. (25) (purple solid line), except at the smallest value of d/R where the truncation to the first order shows its limitations. The error bars represent a confidence interval of our measurements and are obtained from the velocity difference, converted in relative units, between the adaptive case and in the no-slip case at $d/R = 10$, for which we expect maximum accuracy.

approximation, simulations results are in fairly good agreement with the theoretical estimate of the settling velocity of the particle provided by the method of reflections [39], computed at the first reflection, given by

$$\frac{U_P}{U_0} = 1 + \frac{3R}{2d}, \tag{25}$$

where R is the radius of the spheres and d is the distance between their centers. Results as shown in Fig. 5.

A. Accuracy as a function of the simulation box size at fixed resolution

The adaptive boundary conditions, proposed in the previous paragraph, are now applied to measure the performance of the BB and the EI fluid-solid interaction schemes in reproducing the dynamics of the settling of a spherical particle in Stokes flow conditions.

In this first analysis we evaluate the impact of different simulation box sizes L on the accuracy of the particle terminal velocity, computed as the percentage deviation from the Stokes settling velocity given by Eq. (24). Simulations are performed with particle radius $R = 10$, Reynolds number $Re = 10^{-3}$, and a value of $\tau = 0.6$ is chosen in order to reduce as much as possible the onset of numerical slip effects. The Kn number given by Eq. (8) is now calculated using the particle radius as characteristic length scale. In this way $Kn \sim 0.07$ for $R = 1$ and $Kn = 0.007$ for $R = 10$. The density of the particle is set to $\rho_p = 2\rho_f$ and the gravity acceleration along the z direction $-g$ applied on the particle follows from the choice of $Re = U_0 R/\nu$ and using Eq. (24). The time-averaged settling velocity $\langle U_P \rangle$ is computed after the initial transient required to reach the terminal velocity has decayed, and then compared with the Stokes value from Eq. (24).

While the distance between the simulation boundaries and the particle is still playing a relevant role on particle dynamics, we are now able to isolate the accuracy loss induced by finite-resolution effects due to particle discretization from domain size effects. These results are highlighted in Fig. 6, where we plot the relative error of the average of the particle terminal velocity for different simulation domain sizes L. We observe that the accuracy on the particle velocity converges to a nonzero value that we interpret as the maximum precision achievable for a given particle resolution and for a virtually unlimited simulation domain size, for which all the nonideal effects induced by the finite size of the simulation domain will vanish and only the resolution error will remain. In order to exclude, as much as possible, boundary effects on the accuracy estimation, we extract the convergence value through a power-law fit of the form

$$f(L) = \left(\frac{1}{L}\right)^{\alpha} + \varepsilon, \tag{26}$$

where α and ε are free fit parameters.

The accuracy loss induced by the presence of the simulation boundaries for large confinement ratios $2R/L$ can be understood by recalling the general theory of multipoles expansion (e.g., Chap. 3 in [39]) for the velocity field generated by an arbitrary shaped particle. First, since the simulated

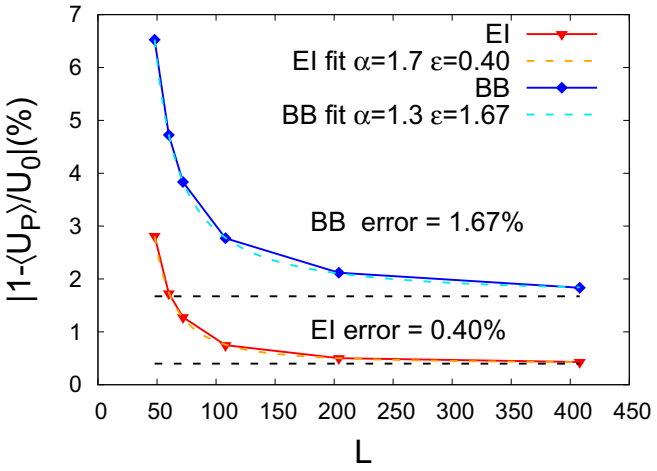

FIG. 6. Accuracy of the particle terminal velocity using EI (red triangles) and BB (blue diamonds) boundary conditions for $R = 10$, $\tau = 0.6$, and $Re = 10^{-3}$ obtained varying the simulation domain size L from 48 to 408. Fit functions obtained using Eq. (26) (colored dashed lines) show a convergence of the error to a limit value (black dashed lines) represented by the fit parameter ε. This limit value represents the maximum accuracy achievable for a given particle resolution.

particle is not an ideal sphere due to finite-resolution effects related to the modeling of the particle surface within the LBM, the perturbation induced on the flow will deviate from the one of an ideal sphere. Second, an additional source of error is given by the model used to describe moving boundary effects embodied in Eqs. (13) and (14), where the velocity profile between particle surface and the first adjacent fluid node is assumed linear, which we know from Eq. (19) is not the case for the problem under examination.

As a result of these two error sources, deviations from Stokes analytical solution are expected in the vicinity of the particle, as shown in Fig. 7, where the relative error of the flow is computed for every fluid node as

$$e_u = \sqrt{\frac{|u_{\mathrm{an}}(U_P) - u_{\mathrm{sim}}|^2}{u_{\mathrm{an}}^2(U_P)}}, \tag{27}$$

where the analytical velocity field $u_{\mathrm{an}}(U_P)$ is calculated from Eqs. (15) and (19) using the instantaneous velocity U_P of the particle.

If the boundaries of the simulation domain are too close to the particle, the higher order terms in the flow field generated by nonideal effects related to particle discretization will not vanish and the match with the analytical solution for a settling sphere forced on the domain boundaries will not be perfect, negatively affecting the simulation accuracy.

B. Convergence analysis and velocity fluctuations

In the previous paragraph we showed how to measure the asymptotic error for a particle at fixed radius. The same analysis shown in Fig. 6 is now repeated for different values of R in order to obtain the accuracy convergence rate with respect to particle resolution. For each investigated value of R we performed different simulations varying the domain size L

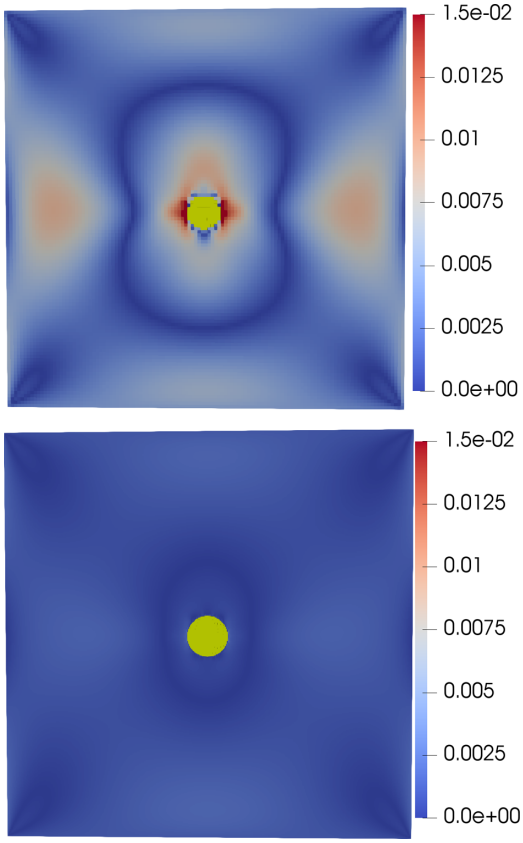

FIG. 7. Relative error in the flow as defined in Eq. (27), $e_u = \sqrt{|u_{\mathrm{an}}(U_P) - u_{\mathrm{sim}}|^2 / u_{\mathrm{an}}^2(U_P)}$, for a less resolved (top) and better resolved (bottom) particle with respectively $R = 5$ and $R = 20$ at the same confinement ratio $2R/L$. The analytical velocity field $u_{\mathrm{an}}(U_P)$ is computed using Eqs. (15) and (19). Discretization effects induce higher deviation from the ideal Stokes flow field around the particle that strongly depend on particle resolution.

in order to fit the measured error with Eq. (26) to obtain the asymptotic error.

In addition to the average deviation of the particle velocity from the Stokes solution, velocity fluctuations around the mean velocity represent another important observable to access particle dynamics accuracy. While the particle moves across the lattice grid, its total volume varies accordingly to the lattice nodes that are covered (and uncovered) by the particle during its motion. These volume fluctuations are reflected in the particle dynamics by unphysical jumps in the velocity profile, as shown in Fig. 8, where the time evolution of the velocity of the particle is plotted. We compute the average velocity fluctuations as

$$\langle \Delta U_P \rangle = \frac{\sum_t (U_{P,t} - \langle U_P \rangle)^2}{T}, \tag{28}$$

where t represents a measure at a given time step and T the total number of time steps, both taken excluding the initial transient.

Results obtained from the convergence analysis of the two investigated models (BB and EI) are compared in Fig. 9, where the measured asymptotic error and the average velocity fluctuations are plotted against the particle radius. All the simulations have been performed by keeping $\tau = 0.6$, $\rho_p =$

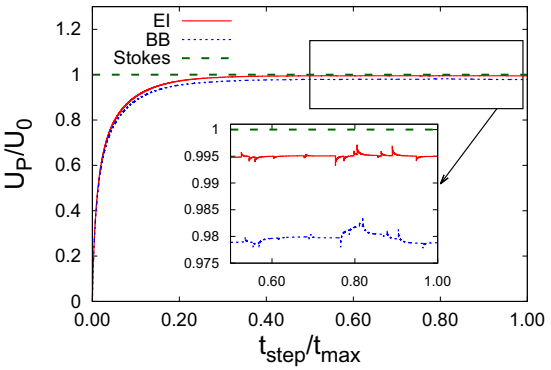

FIG. 8. Velocity U_P of a settling particle with $R = 10$, normalized with respect to the Stokes settling velocity U_0 using the EI (red solid line) and the BB (blue dashed line) schemes, as a function of time. Other relevant parameters are $L = 200$, $\tau = 0.6$, $\rho_p = 2\rho_f$. In the inset a zoom on the y axis of the selected region is performed to show the fluctuations in the velocity profile due to the volume variation of the particle during its motion.

$2\rho_f$, $Re = 10^{-3}$. After a best fitting of the data we obtain an empirical relation for the asymptotic error given by

$$\varepsilon_{\mathrm{BB}}(R) = 13.7\,R^{-0.89}, \tag{29}$$

$$\varepsilon_{\mathrm{EI}}(R) = 13.7\,R^{-1.51}. \tag{30}$$

While for the EI scheme the measured convergence rate is in fair agreement with the one observed for fixed particles in [22], for the BB case the second-order scaling shown in [22] is lost and now it exhibits a clear first-order scaling. The main difference between our case and the reference one is the motion of the particle: EI is able to continuously detect the boundaries location while the position of the particle is updated, while BB can detect an update in the boundary locations only after a displacement of the particle of the order of the lattice spacing, resulting in a first-order accurate description of the boundary motion. Velocity fluctuations are second-order convergent for both investigated cases.

There are other concurring mechanisms that have a detrimental effect on the accuracy of particle dynamics: at first, lattice parameters such as the relaxation time τ are known to influence the LBM accuracy in recovering the hydrodynamics of the flow [41], so that a different choice of τ can lead to a different accuracy scaling. Another relevant error source is the already discussed model for the interaction between the flow and a moving boundary embodied in Eqs. (13) and (14), which introduces a first-order error in the flow velocity around the particle.

C. Complete interpolation: Subgrid particle simulations and accuracy

In the standard momentum exchange approach, the link nodes (i.e., fluid nodes from which at least one lattice velocity component $\mathbf{e}_a$ points inside the solid volume) are evaluated only between fluid and solid nodes, neglecting the possibility to detect the surface of the particle when it is located between two fluid nodes. While, in general, this feature is not particularly important for fully resolved spherical particles, it

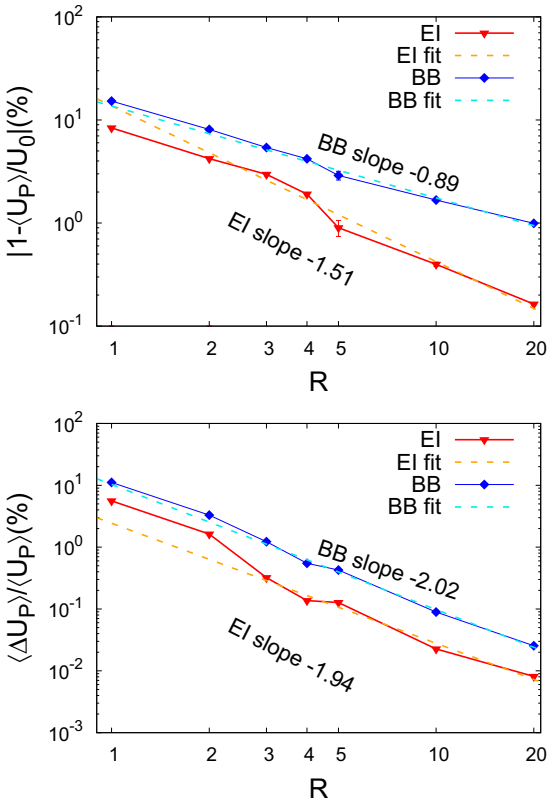

FIG. 9. Asymptotic error (top) of the average velocity $\langle U_P\rangle/U_0$ and average velocity fluctuations $\langle\Delta U_P\rangle/\langle U_P\rangle$ as computed from Eq. (28) (bottom), with respect to particle radius R. Convergence rates are obtained through a power-law fit (colored dashed lines) of the measured asymptotic error and reported as the slope of the best fit in the semilog plot. EI strongly reduces errors, keeping an accuracy scaling comparable with the one observed in [22]. Using BB, the accuracy scaling is instead only first order. Second-order convergence is maintained in both cases for the velocity fluctuations.

can introduce an important effect for particles with complex shapes or with fine surface details. In this section we propose an improvement of the EI scheme in which the capability to detect the surface of the particle also in between two fluid nodes is implemented using a standard ray-sphere intersection algorithm [38] as shown in Fig. 1. This boundary treatment will be addressed as complete equilibrium interpolation (CEI).

One example of the capability to resolve subgrid particle dynamics offered by CEI is shown in Fig. 10 where the settling of a particle with radius $R = 0.6$ initialized in the center of the simulation domain is compared with the EI scheme for two different lattice models, namely the D3Q19 and D3Q27 lattice stencils. An increased number of velocities, provided by a larger lattice, can increase accuracy of CEI in detecting the surface of the particle. This effect can be observed in the top plot of Fig. 10, where the number of links is plotted as a function of time. It is to be noted, however, that on-grid particle description only allows us to use single-cells lattice stencils, so that the D3Q27 is already the upper limit.

The achievable accuracy for small radii, i.e., when $R \leqslant 2$, using a CEI scheme is now investigated and compared with the standard EI and BB models for a D3Q19 lattice stencil.

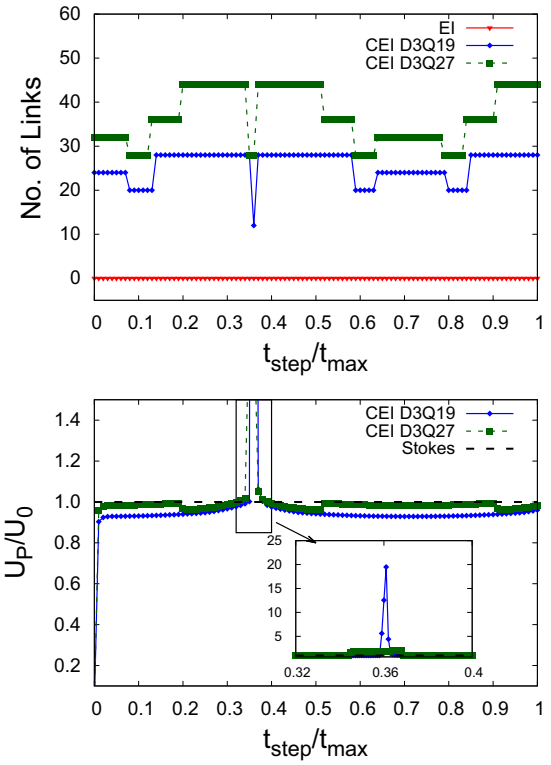

FIG. 10. Number of link nodes for momentum exchange (top) and time evolution of particle velocity (bottom); EI (red triangles), CEI using D3Q19 lattice (blue diamonds), and CEI using D3Q27 lattice (green squares) for a particle with radius $R = 0.6$. Standard EI is not able to capture a subgrid particle when initialized in the domain center (zero occupation on top plot), leading to a free fall velocity profile (and thus omitted from the bottom plot for the sake of readability). Using CEI, the particle is correctly detected, but some peaks appear in the velocity profile due to the drop in the number of link nodes during the motion of the particle when a D3Q19 lattice is used. This effect can be mitigated by using the higher order lattice such as D3Q27.

The simulations are performed by keeping the confinement ratio $2R/L = 0.05$ between particle radius R and the size L of the computational box, which is enough to keep the effects from the boundaries of the simulation box negligible when compared to the ones from the particle resolution for such small radii. The relaxation time is again set to $\tau = 0.6$, while the density of the solid particle is increased to $\rho_p = 3\rho_f$ to increase numerical stability against the stronger fluctuations observed in the simulation due to the extreme values of R.

For such small particles the discrete effects introduced by the simulation grid can play an important role on the dynamics, so we addressed the problem by performing an ensemble of ten identical simulations with different initialization of the particle center, that now is randomly located in the range of ± 0.5 with respect to the simulation domain center, as sketched in Fig. 11.

In this way the particle discretization on the lattice grid will be different for every different location of the particle center, allowing us to observe the impact of the lattice on the overall accuracy.

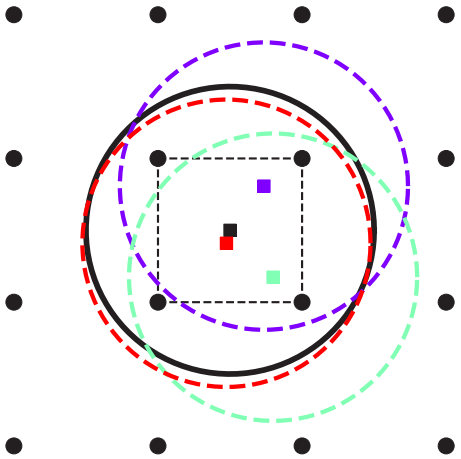

FIG. 11. Sketch of particles with $R = 1$ initialized with random offsets of ± 0.5 with respect to a particle (black solid line) located at the center of the simulation domain (black square). The colored squares represent the center of each different particle (dashed colored lines). Different initializations lead to different discretizations of the particles on the lattice grid, represented by the number of lattice nodes connected by the black dashed lines that are enclosed by the surface of the particles.

Results are shown in Fig. 12, where the final accuracy and velocity fluctuations, averaged over the ensemble, are plotted against the particle radius R. In addition, minimum and maximum values, observed in the ensemble, are reported as error bars in order to give a quantitative idea of the fluctuations that can occur for such small particles using an on-grid description.

It is remarkable that using the CEI scheme it is possible to keep the average error on particle speed below 10% for subgrid particles, while strongly suppressing velocity fluctuations of more than one order of magnitude in these cases. The performance scaling of the momentum exchange routine with respect to particle resolution has been investigated in Fig. 13. It is found that the overhead introduced by CEI, noticeable only for large radii, is small if compared with the increase in accuracy provided by the CEI scheme. From Fig. 12 it can be noted, in fact, that for the case of a particle with $R = 1$ the accuracy obtainable with the CEI scheme is higher than the one achievable with the BB scheme using $R = 2$, while the computational overhead is barely noticeable. Moreover, if the same reduction in resolution is applied also to the domain size, like in convergence studies, a shrinking of a factor of 2 in the overall resolution can lead to an improvement in the performances up to a factor of 8 in terms of simulation time.

IV. ROTATIONAL DYNAMICS OF A SPHEROIDAL PARTICLE IN A SHEAR FLOW

In this section we investigate the dynamics of spheroidal particles set into rotation by a shear flow. In the first part of the analysis we show an application of the adaptive boundary conditions to the case of spherical and ellipsoidal particles free to rotate in an ambient shear flow, while in the last part we study the accuracy of the CEI scheme in resolving the rotational dynamics of an ellipsoidal particle. The relaxation

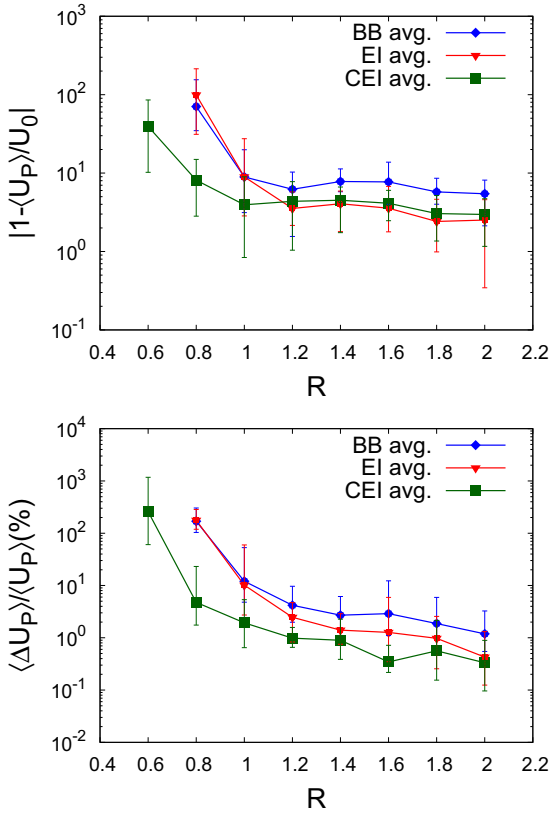

FIG. 12. Averages (solid lines) of the accuracy on particle velocity (top) and of the velocity fluctuations (bottom) for $0.6 \leqslant R \leqslant 2$. Results are averaged over an ensemble of ten simulations having different random initialization of the particle center within ± 0.5 from the domain center. Minimum and maximum values within the ensemble are represented by the error bars. The CEI scheme (green squares) allows us to describe the dynamics of particles with small radii at increased accuracy with respect to EI (red triangles) and BB (blue diamonds) schemes, while strongly reducing velocity fluctuations. With the CEI scheme it is now possible to detect solid features on the order of one lattice grid spacing.

time is again set to $\tau = 0.6$ for all the simulations in this section.

The angular velocity $\omega(t)$ of a general spheroidal particle set into motion by an unbounded shear flow is described in the work of Jeffery [42] as

$$\omega(t) = \frac{C}{a^2 + b^2}[a^2 \cos^2\theta(t) + b^2 \sin^2\theta(t)], \tag{31}$$

$$\tan\theta(t) = \frac{a}{b}\tan\left[\frac{Cabt}{a^2 + b^2}\right], \tag{32}$$

where a and b are the major and minor axes of the ellipsoid in the plane of the shear, respectively, and $C = 2U_{\text{shear}}/L$ is the shear rate at a given simulation domain size L, assuming that the shear flow is driven by two moving walls at $\pm U_{\text{shear}}$. The variable $\theta(t)$ describes the angle between the major axis and one of the main directions in the shear plane. The angular velocity $\omega(t)$ of the ellipsoid is then described by a family of curves that depend on the shear rate and on the starting orientation of the particle and in general it will show periodic

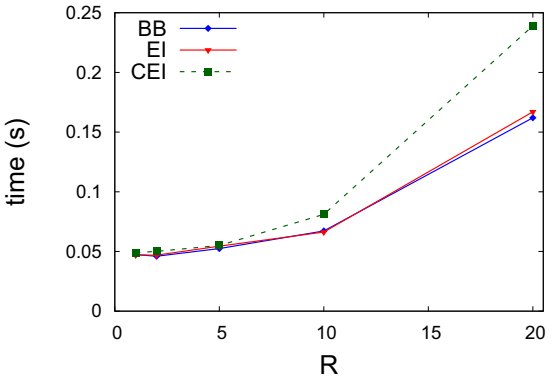

FIG. 13. Time required to perform one call of the momentum exchange routine, averaged over 1000 time steps, for BB (blue diamonds), EI (red triangles), and CEI (green squares) as a function of the particle radius R. For small values of R the performances of the three investigated algorithm are similar, while for larger values of R CEI introduces some overhead that can be reduced with a higher level of code optimization.

oscillations with period

$$T_{\text{jef}} = \frac{\pi(a^2 + b^2)}{abC}. \tag{33}$$

Two particular cases are shown in Fig. 14, where the analytical trajectory of the angular velocity is plotted for a sphere and for an ellipsoid with internal aspect ration $a/b = 2$.

The adaptive boundary conditions presented in the previous section, i.e., the possibility to enforce on the boundaries of the simulation box the analytical expression of the perturbation induced by the presence of the particle, can be straightforwardly applied for the case of a spherical particle free to rotate in a shear flow. An unperturbed shear flow can be modeled as the sum of two equal contributions from an ambient vorticity $\mathbf{\Omega}^{\infty}$ and an ambient strain $\mathbf{E}^{\infty}$. The velocity field of a shear flow having a velocity of $\pm U_{\text{shear}}$ along the $\hat{x}$ direction at $y = \pm L/2$, respectively, can then be obtained from Eq. (15) by imposing the ambient fields as

$$\mathbf{\Omega}^{\infty} = \left(0, 0, -\frac{C}{2}\right), \tag{34}$$

$$\mathbf{E}^{\infty} = \begin{pmatrix} 0 & \frac{C}{2} & 0 \\ \frac{C}{2} & 0 & 0 \\ 0 & 0 & 0 \end{pmatrix}. \tag{35}$$

In this configuration the rotational dynamics of the particle is limited to the shear plane and the angular velocity of the particle can be written as $\boldsymbol{\omega}_P = (0, 0, \omega_P)$. For this reason, from now on we will refer only to the nonzero component ω_P and the vector notation will be omitted.

As we did for the settling problem, the particle and flow dynamics are fully solved by the PR-LBM and the instantaneous value of the particle angular velocity ω_P is used to impose the analytical flow using Eq. (15) on the boundaries of the simulation domain. In this way we are able to suppress any boundary effects due to the finite size of the simulation domain also for extreme cases, as shown in Fig. 15, where we plot the angular velocity of a spherical particle with $R = 10$ initialized in the center of a domain with size $L = 24$ (which

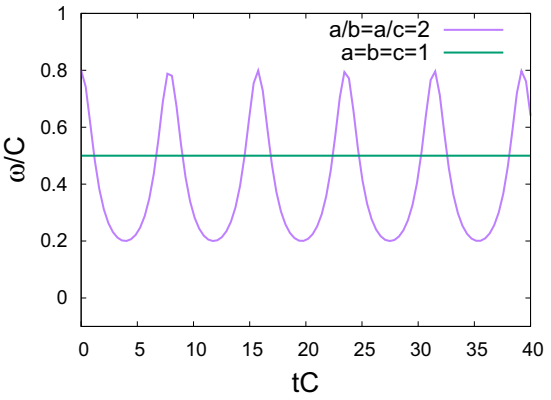

FIG. 14. Analytical prediction given by Eq. (31) of angular frequency as a function of time of an ellipsoid with $a/b = a/c = 2$ originally oriented with the major axis a parallel to the flow and a sphere with $a/b = a/c = 1$. The x and y axis are normalized with respect to the shear rate $C = 2U_{\text{shear}}/L$.

means that the confinement ratio $2R/L \sim 1$). We compare the results using our adaptive method and the standard approach (i.e., when the shear flow is driven by walls moving at $\pm U_{\text{shear}}$ and periodic boundary conditions are applied along the direction of the flow). The exact angular frequency for the particle, as predicted by Eq. (31), is obtained for any values of the particle radius and domain size, so that a resolution analysis for the spherical particle case is omitted. While in principle Eqs. (20)–(23) are exact only for a spherical particle, the adaptive boundary treatment can be efficiently used to reduce boundary effects also for the case of a nonperfectly spherical particle. We focus on the case of an ellipsoid with internal aspect ratio $a/b = a/c = 2$ and major radius $a = 10$, rotating in a shear flow with analogous geometry as the one used for

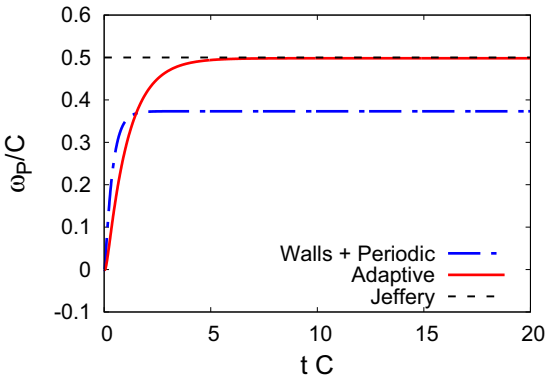

FIG. 15. Angular velocity for a sphere of radius $R = 10$, rotating in a shear flow with shear rate $C = 0.002$. The simulation domain size is set to $L = 24$, so that the domain boundaries of the simulation box are almost in contact with the particle. Using the adaptive boundary conditions (red solid line) we are able to suppress detrimental boundary effects and the analytical angular frequency (black dashed line) is exactly reproduced. Using a standard approach (blue point-solid line) consisting of no-slip moving walls in the orthogonal direction to the flow and periodic boundaries along the flow the detrimental effects due to the vicinity of walls on Jeffery's ideal dynamics is evident.

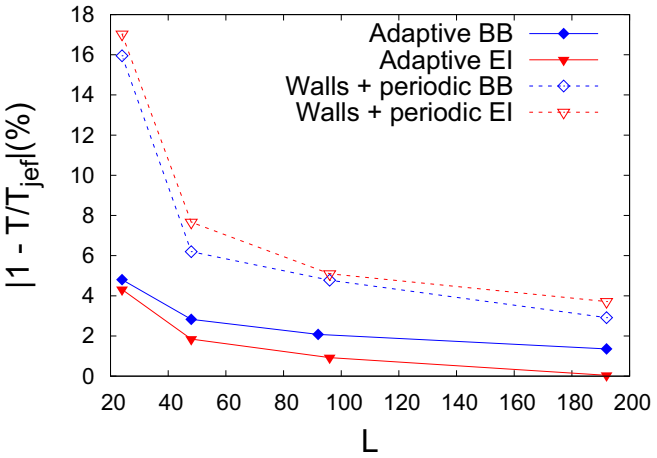

FIG. 16. Relative error on the analytical period, given by Eq. (33) and measured by fitting our data with Eqs. (36) and (37), of the oscillations of the angular frequency for an ellipsoid with aspect ratio $a/b = a/c = 2$, at fixed major radius $a = 10$ for different values of the simulation domain size L. We compare the results using the BB (blue diamonds) and EI (red triangles) schemes for two different treatments of the simulation domain boundaries. The influence on the dynamics of the particle of the simulation boundaries is strongly reduced using our adaptive treatment. Results for $\tau = 0.6$, $U_{\text{shear}} = 0.01$.

Fig. 15. The shear rate C is set in such a way that $U_{\text{shear}} = 0.01$ is fixed for all the simulations. In this context we apply the adaptive treatment on the boundaries using Eqs. (20)–(23), but this time we use an effective radius for the perturbations given by $R_{\text{eff}} = \sqrt[3]{abc}$. This is equivalent to approximate, on the simulation boundaries, the perturbation generated by the rotating ellipsoid with the ones generated by a sphere with the same volume. We compare the performance in recovering the analytical period from Eq. (33) using our adaptive approach and the standard approach, for different confinement ratios $2a/L$, and the results are shown in Fig. 16. In order to perform this measurements we fit our data with a modified set of Eqs. (31) and (32), which are now able to capture period variations and to take into account the presence of an initial transient. These equations read

$$\omega_{\text{fit}}(t) = \frac{C}{a^2 + b^2}[a^2 \cos^2\theta_{\text{fit}}(t) + b^2 \sin^2\theta_{\text{fit}}(t)], \tag{36}$$

$$\tan\theta_{\text{fit}}(t) = \frac{a}{b}\tan\left[\frac{Cabt}{a^2 + b^2}s + \phi\right], \tag{37}$$

where s and ϕ are free fit parameters that represent a period stretching and a phase shift due to an initial transient, respectively. While it is commonly found in the literature [43,44] that in this setup boundaries effects induced by triggering the shear flow using moving walls can be considered negligible for a confinement ratio $2a/L \leqslant 0.1$, we observe that we can largely reduce their impact using our adaptive approach for all the investigated confinement ratios.

We now aim to test and compare the CEI scheme capabilities to model particles with more complex shapes. This is done by comparing the performances of different boundary treatments of the surface of the particle in reproducing the

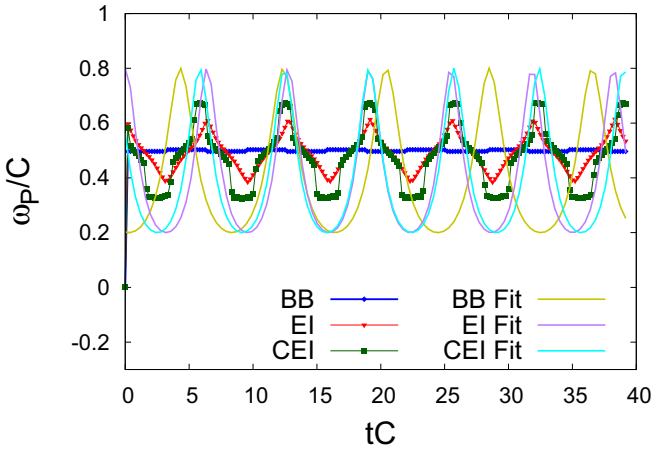

FIG. 17. Angular frequency evaluated from Eq. (31) using BB (blue diamonds), EI (red triangles), and CEI (green squares) schemes for an ellipsoidal particle with major radius $a = 1.5$ and minor radii $b = c = 0.75$ at $\tau = 0.6$ and $L = 30$. The particle center is initialized at the point (15,15,15). For the BB case the algorithm is not able to distinguish the ellipsoid from a spherical particle, while the EI and CEI schemes are increasingly better in capturing shape features. The best fits, obtained using Eqs. (36) and (37), are used to evaluated the accuracy of every method in reproducing the ideal rotational dynamics.

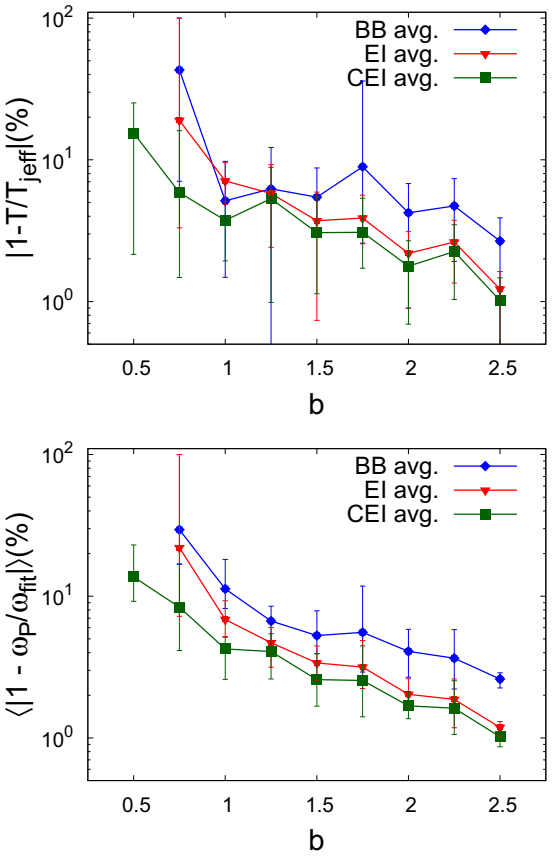

FIG. 18. Error on the period (top plot) and error on the trajectory of the angular frequency (bottom plot) of an ellipsoid rotating in a shear flow. The ellipsoid has internal aspect ratio $a/b = a/c = 2$, where a is the major axis and $b = c$ are the minor axes. The resolution of the ellipsoid ranges between $0.5 \leqslant b \leqslant 2.5$. Results are averaged over an ensemble of ten simulations, each with a different offset of the position of the particle from the domain center. The confinement ratio between particle major axis and simulation domain is kept constant, with $2a/L = 0.1$. While EI (red triangles) provides better accuracy with respect to BB (blue diamonds), both methods fail in detecting a particle with $a = 1$ and $b = 0.5$, where CEI (green squares) succeeds. The latter leads to a general improved accuracy with respect to EI. The error bars represent the minimum and maximum value in the ensemble.

dynamics of an ellipsoid rotating in a shear flow. To simulate this setting we again use the adaptive treatment by enforcing on the simulation boundaries Eqs. (20)–(23), where the perturbation terms are approximated by the ones produced by a sphere rotating at ω_P with the effective radius $R_{\text{eff}} = \sqrt[3]{abc}$, in an analogous way as we did for Fig. 16. The shear rate C is again set to reproduce the shear flow produced by two walls moving at $\pm U_{\text{shear}}$, with $U_{\text{shear}} = 0.01$.

Simulations have been performed for an ellipsoid with internal aspect ratio $a/b = a/c = 2$, while varying the radii of the particle and the simulation domain size L in order to keep the confinement ratio constant at $2a/L = 0.1$.

An example of the improvement introduced by interpolation based algorithms is shown in Fig. 17, where the angular velocities of a low resolution particle are compared for different boundary treatments. The EI scheme already leads to a remarkable improvement with respect to the BB scheme, but now using the more sophisticated CEI scheme the ellipsoid poles are better resolved during the dynamics, leading to a more defined trajectory. The algorithm capabilities to capture particle dynamics for a progressively less resolved ellipsoid can now be addressed. We investigate how the error scales with the resolution of the particle by varying a from 1 to 5. As we did for the case of the settling of a spherical particle, we address the problem of the impact of grid resolution on the simulation accuracy by repeating ten identical simulations for different random initialization of the particle center within a range of ± 0.5 with respect to the simulation domain center.

The error on the period is once again measured using Eqs. (36) and (37). It is to be noted, however, that the error on the period is not the best indicator to finely address the accuracy of the dynamics of a low resolution particle, since the fit model embodied by Eqs. (36) and (37) can often extract an accurate angular trajectory also from not so accurate signals, as shown for the BB case in Fig. 17. For this reason here we consider also the average error on the angular trajectory between the simulation data ω_P and the fit function ω_{fit} obtained from Eq. (36). In this way we are able to provide a more reliable indicator of the instant-by-instant precision in the reconstruction of the rotational dynamics of the ellipsoid under examination.

Results are shown in Fig. 18, where the error on the period and the average error on the angular trajectory, as well as their maximum and minimum values, are plotted for the BB, EI, and CEI schemes and different values of particle resolution. Improvements introduced by interpolation schemes are evident, with the maximum accuracy obtained through CEI, that allows us now to capture particles radii small as half of the

grid spacing. It is interesting to note, by comparing Fig. 18 with Fig. 12, that the improvements introduced by the CEI scheme are slightly more evident when an ellipsoidal particle is used, showing that CEI is more effective for particles with a complex shape.

V. CONCLUSIONS

In conclusion, in this work we propose an accurate and efficient method, based on an adaptive boundary treatment, to strongly suppress boundary effects due to the finite size of the simulation domain on the dynamics of spherical and ellipsoidal particles free to move in an unbounded fluid under Stokes flow conditions. This is done by enforcing the ideal Stokes flow solution on the simulation domain boundaries for an unbounded domain, accordingly to the instantaneous particle velocity as solved by the Lattice-Boltzmann simulation. In a sense, our approach allows us to impose the correct boundary condition at infinity, but at a finite distance instead.

We first show that through this treatment of the boundaries of the simulation domain we are able to reproduce the ideal Stokes dynamics in two cases of interest, i.e., the settling of a spherical particle under gravity and the rotation of a spherical and ellipsoidal particle in a shear flow, with a higher precision with respect to the standard approaches.

We then isolate the influence of particle resolution by performing fine measurements of the accuracy convergence of the particle dynamics in the aforementioned problems, down to very low resolutions. It is the first time, to our knowledge, that an accurate evaluation of the accuracy of the particle is carried down to such low resolutions in cases where the particle is free to move across the lattice grid.

Particle translational accuracy is firstly measured for two widely used fluid-solid interaction models, namely bounce-back (BB) and equilibrium interpolation (EI), showing that the latter strongly improves accuracy while reducing velocity fluctuations. Under the investigated case, measured convergence rate for the EI scheme is in fair agreement with what is found in the literature for a fixed obstacle, while the BB scheme only exhibits a first-order convergence due to the lower accuracy in capturing the dynamics of moving boundaries.

Finally, we propose a third model as an extension of EI called complete equilibrium interpolation (CEI) that allows us to detect momentum exchange also between two fluid nodes, in the case in which the particle surface is occupying a position between the two. We show that CEI is not only able to detect particles as small as one lattice grid spacing, where the BB and EI schemes fail, but also to provide an higher accuracy in cases where the particle size is only a few lattice nodes, while strongly suppressing velocity fluctuations due to particle volume change during time evolution.

We find that these improvements are more evident for elongated particles such as ellipsoids, making this model promising for the modeling of particles with complex shapes (i.e., needles) or with small features at their surface. Another relevant application of this method is the simulation of dense suspensions of particles, since it allows us to increase the number of simulated particles without a large accuracy loss, potentially increasing computational efficiency.

We finally show that complete equilibrium interpolation is capable to recover correct flow results when inertial effects are relevant for the dynamics of the particle (Appendix A).

As a last note, the adaptive domain boundary treatment presented in this paper can find relevant applications as an improvement to the standard periodic boundaries in all the cases where a spherical or quasispherical particle or bubble is moving in an ambient flow under Stokes conditions, such as in jetting problems or transport of droplets in aerosols, and it can be further extended to address more complex shapes and number of particles.

ACKNOWLEDGMENT

This work was supported by the Netherlands Organization for Scientific Research (NWO), under the Project No. 15376.

APPENDIX A: RECOVERING EFFECTS OF INERTIA AT FINITE REYNOLDS NUMBERS

In this Appendix we investigate the capability of CEI and EI to recover the correct results in cases where inertia is relevant on the dynamics of the particle, focusing first on the problem of a cylindrical particle settling in a vertical channel at $Re = 1.03$ and $Re = 8.33$, and later on the problem of a cylindrical particle rotating in a shear flow at $Re = 79.6$. The 2D nature of this class of problems and the presence of finite Reynolds numbers are the reasons why this investigation is addressed as an Appendix, since in the main text we focus on 3D flows in the Stokes regime.

In the absence of inertia, a particle released away from the center of a vertical channel would settle straight down with no lateral motion [40]. This is no longer the case when inertia becomes important, as particle migrates horizontally until the final equilibrium position is reached at the center of the channel. This class of phenomena has been extensively investigated by a number of authors through different numerical schemes such as the finite-element method [45–47] and the LBM [48–50]. In the first part of this Appendix we investigate the performances of EI and CEI with respect to BB to recover the expected dynamics under the same flow conditions as Li *et al.* [48] [the simulation setup is sketched in Fig. 19(a)].

The channel width (along the $\hat{x}$ direction) is set to $L = 8R$, where R is the particle radius; the particle is released at an horizontal position of $x = 0.19L$ and it is free to settle under the effect of a body force $\mathbf{g} = (0, 0, g)$. The relaxation time and the particle density are set to $\tau = 0.6$ and $\rho_p = 2\rho_f$, respectively. The body force $\mathbf{g}$ is tuned to match with the desired Reynolds numbers of $Re = 1.03$ and $Re = 8.33$, where $Re = U_P 2R/\nu$ and U_P is the final settling velocity of the particle. We apply uniform zero velocities at the inlet and zero normal derivative of the velocity at outlet.

Using a fully resolved particle with $R = 12$ the results from [48] are recovered with very high accuracy as shown in Fig. 20.

From the same plot (Fig. 20) it can be also observed that using EI and CEI the particle tends to respond slightly slower in the transient when compared with the BB results. This effect can be related to the increased accuracy at which EI and CEI can capture inertial effects with respect to BB and the

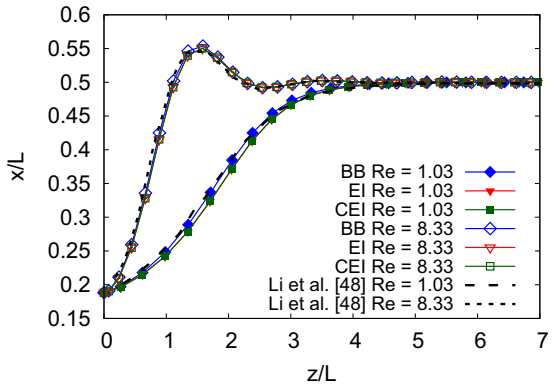

FIG. 20. Settling trajectory of a cylinder released at $x = 0.19L$ of a vertical channel at $Re = 1.03$ and $Re = 8.33$. The particle radius is $R = 12$, while the channel width $L = 8R$. The horizontal migration towards the center of the channel is an effect related to the inertia of the particle. The dynamics observed by Li *et al.* [48] (black dashed lines) is correctly reproduced with all the investigated boundary schemes (colored point lines). Other relevant simulation parameters are $\tau = 0.6$ and $\rho_p = 2\rho_f$.

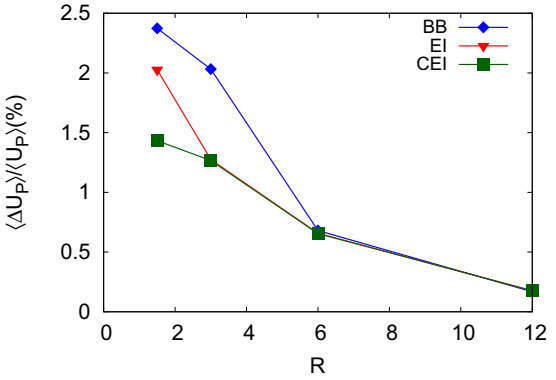

FIG. 21. Average velocity fluctuations $\langle \Delta U_P \rangle$ [as defined in Eq. (28)] of the terminal velocity U_P of a cylinder settling in a vertical channel as a function of its radius R for BB (blue diamonds), EI (red triangles), and CEI (green squares). The particle is released at $x = 0.19L$ of a channel with width $L = 8R$ at $Re = 1.03$. EI and CEI slightly reduce the velocity fluctuations related to the volume fluctuations of the particle, but the effect is noticeable only for small values of R.

stress-integration method proposed in [48]. These differences are, in any case, very small.

Furthermore, we investigate the accuracy in recovering the final horizontal position for different resolutions of the system as a function of the particle radius R at fixed Reynolds number $Re = 1.03$. It is found that the correct horizontal position of the particle is recovered with very high precision for all the investigated combinations of resolution and boundary schemes. Interpolation-based schemes only provide a small improvement in the velocity fluctuations of the final settling velocity for small radii as shown in Fig. 21.

In the last part of this Appendix we show that EI and CEI are able to reproduce the correct flow dynamics of a cylinder freely suspended and free to rotate in a shear flow. Following the simulation setup presented by Ding and Aidun [51], and sketched in Fig. 19(b), the radius of the particle is initially set to $R = 64$ and it is initialized in the center of a channel with a size of $34R \times 4R$, so that the channel width along the $\hat{y}$ direction is set to be $L = 4R$. The relaxation time and the particle density are set to $\tau = 1$ and $\rho_p = \rho_f$, respectively. The shear flow is generated by two opposite walls located at $y = \pm L/2$ and moving with a velocity $\pm U_{\text{shear}}$. The velocity of the walls is tuned to have $Re = CD^2/\nu = 79.6$, where D is diameter of the cylinder and $C = 2U_{\text{shear}}/L$ is the already defined shear rate. This setup is in agreement with the experiments of Zettner and Yoda [52].

The simulation results are presented in Fig. 22, and they show a good agreement with the experimental data presented in [52], confirming that for large resolution of the particle BB, EI, and CEI recover identical results.

By performing the same simulations at different resolutions, down to $R = 4$, we observed that good accuracy is

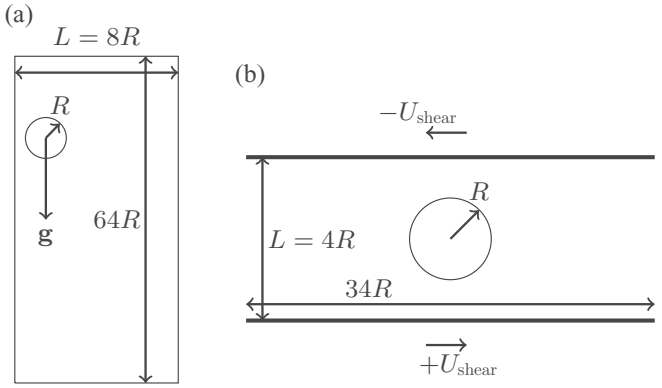

FIG. 19. Schematic representation of (a) a cylindrical particle of radius R released near one wall of a two-dimensional channel set into motion by a gravity force **g**, and (b) a cylindrical particle free to rotate in a shear flow.

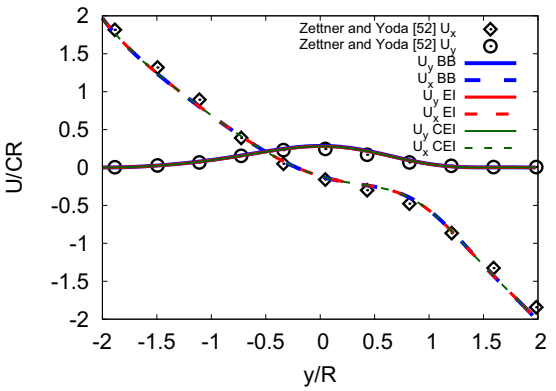

FIG. 22. The $\hat{x}$ (dashed lines) and $\hat{y}$ (solid lines) velocity components U_x and U_y of the flow versus y/R at the domain section $x/R = -1.8467742$ from a rotating cylinder with radius $R = 64$ centered at (0,0). The Reynolds number is $Re = 79.6$. The same simulation is performed using BB (blue), EI (red), and CEI (green) and numerical results are in good agreement with the experimental data from Zettner and Yoda [52] (black circles and diamonds) for all the investigated schemes.

always recovered for all investigated boundary schemes until a critical resolution limit is reached. Below this threshold the flow is clearly under resolved and the algorithm is unable to capture the correct hydrodynamics for the simulated *Re*.

The weak relation between the accuracy of the dynamics and the resolution of the particle observed in this Appendix is partially related to the strong symmetry of the investigated systems, combined with the more strict requirements in terms of fluid resolution needed to simulate higher *Re* numbers. This last aspect suggests that low-Reynolds number conditions provide a better test case to access resolution effects related to particle discretization.

APPENDIX B: LATTICE WEIGHTS AND HERMITE POLYNOMIALS

In this Appendix we provide the values of the lattice velocities $\boldsymbol{e}_a$ and relative weights w_a for the D3Q19 and D3Q27 lattice stencils, followed by the explicit expression of the Hermite polynomials required for the full second-order expansion of the PR-LBM adopted in this work:

$$\boldsymbol{e}^{\mathrm{D3Q19}} = [\boldsymbol{e}_0, \ldots, \boldsymbol{e}_{18}] \tag{B1}$$

$$= \begin{bmatrix} 0 & 1 & -1 & 0 & 0 & 0 & 0 & 1 & 1 & -1 & -1 & 1 & -1 & 1 & -1 & 0 & 0 & 0 & 0 \\ 0, & 0, & 0, & 1, & -1, & 0, & 1, & -1, & 1, & -1, & 0, & 0, & 0, & 0, & 1, & 1, & -1, & -1 \\ 0 & 0 & 0 & 0 & 0 & 1 & -1 & 0 & 0 & 0 & 0 & 1 & 1 & -1 & -1 & 1 & -1 & 1 & -1 \end{bmatrix}, \tag{B2}$$

$$\boldsymbol{w}^{\mathrm{D3Q19}} = \left(\frac{1}{3}, \frac{1}{18}, \frac{1}{18}, \frac{1}{18}, \frac{1}{18}, \frac{1}{18}, \frac{1}{18}, \frac{1}{18}, \frac{1}{18}, \frac{1}{18}, \frac{1}{18}, \frac{1}{36}, \frac{1}{36}, \frac{1}{36}, \frac{1}{36}, \frac{1}{36}, \frac{1}{36}, \frac{1}{36}, \frac{1}{36}, \frac{1}{36}\right), \tag{B3}$$

$$\boldsymbol{e}^{\mathrm{D3Q27}} = [\boldsymbol{e}_0, \ldots, \boldsymbol{e}_{26}] \tag{B4}$$

$$= \begin{bmatrix} 0 & 1 & -1 & 0 & 0 & 0 & 0 & 1 & 1 & -1 & -1 & 1 & -1 & 1 & -1 & 0 & 0 & 0 & 0 & 1 & 1 & 1 & -1 & 1 & -1 & -1 & -1 \\ 0, & 0, & 0, & 1, & -1, & 0, & 1, & -1, & 1, & -1, & 0, & 0, & 0, & 0, & 1, & 1, & -1, & -1, & 1, & 1, & -1, & 1, & -1, & -1, & 1, & -1 \\ 0 & 0 & 0 & 0 & 0 & 1 & -1 & 0 & 0 & 0 & 0 & 1 & 1 & -1 & -1 & 1 & -1 & 1 & -1 & 1 & -1 & 1 & 1 & -1 & 1 & -1 & -1 \end{bmatrix}, \tag{B5}$$

$$\boldsymbol{w}^{\mathrm{D3Q19}} = \left(\frac{8}{27}, \frac{2}{27}, \frac{2}{27}, \frac{2}{27}, \frac{2}{27}, \frac{2}{27}, \frac{2}{27}, \frac{1}{54}, \frac{1}{54}, \frac{1}{54}, \frac{1}{54}, \frac{1}{54}, \frac{1}{54}, \frac{1}{54}, \frac{1}{54}, \frac{1}{54}, \frac{1}{54}, \frac{1}{54}, \frac{1}{54}\right.$$
$$\left. \times \frac{1}{216}, \frac{1}{216}, \frac{1}{216}, \frac{1}{216}, \frac{1}{216}, \frac{1}{216}, \frac{1}{216}, \frac{1}{216}\right). \tag{B6}$$

The Hermite polynomials of order n, $\mathcal{H}^{(n)}(\boldsymbol{e})$, up to the second order, read

$$\mathcal{H}^{(0)}(\boldsymbol{e}) = 1, \tag{B7}$$

$$\mathcal{H}_i^{(1)}(\boldsymbol{e}) = e_i, \tag{B8}$$

$$\mathcal{H}_{ij}^{(2)}(\boldsymbol{e}) = e_i e_j - \delta_{ij}, \tag{B9}$$

where δ_{ij} is the Kronecker delta function.

[1] C. Kleinstreuer and Y. Feng, J. Biomech. Eng. **135**, 021008 (2013).

[2] P. Sharma and M. Khare, Transp. Res. D **6**, 179 (2001).

[3] T. D. AlMomani, S. C. Vigmostad, V. K. Chivukula, L. Al-zube, O. Smadi, and S. BaniHani, Crit. Rev. Biomed. Eng. **5**, 427 (2012).

[4] A. K. Bates, M. Rothschild, T. M. Bloomstein, T. H. Fedynyshyn, R. R. Kunz, V. Liberman, and M. Switkes, IBM J. Res. Dev. **45**, 605 (2001).

[5] N. van Doremalen, T. Bushmaker, D. H. Morris, M. G. Holbrook, A. Gamble, B. N. Williamson, A. Tamin, J. L. Harcourt, N. J. Thornburg, S. I. Gerber, J. O. Lloyd-Smith, E. de Wit, and V. J. Munster, N. Engl. J. Med. **382**, 1564 (2020).

[6] S. Asadi, N. Bouvier, A. S. Wexler, and W. D. Ristenpart, Aerosol Sci. Technol. **54**, 635 (2020).

[7] C. K. Aidun and J. R. Clausen, Annu. Rev. Fluid Mech. **42**, 439 (2010).

[8] S. Succi, *The Lattice Boltzmann Equation: For Complex States of Flowing Matter* (Oxford University Press, Oxford, 2018).

[9] L. P. Wang, C. Peng, Z. Guo, and Z. Yu, Comput. Fluids **124**, 226 (2016).

[10] R. M. MacMeccan, J. R. Clausen, G. P. Neitzel, and C. K. Aidun, J. Fluid Mech. **618**, 13 (2009).

[11] S. Melchionna, Macromol. Theory Simul. **20**, 548 (2011).

[12] N.-Q. Nguyen and A. J. C. Ladd, J. Fluid Mech. **525**, 73 (2005).

[13] H. Haddadi, S. Shojaei-Zadeh, and J. F. Morris, Phys. Rev. Fluids **1**, 024201 (2016).

[14] M. Do-Quang, G. Amberg, G. Brethouwer, and A. V. Johansson, Phys. Rev. E **89**, 013006 (2014).

[15] A. T. Cate, J. J. Derksen, L. M. Portela, and H. E. A. Van Den Aakker, J. Fluid Mech. **519**, 233 (2004).

[16] L.-P. Wang, C. Peng, Z. Guo, and Z. Yu, J. Fluids Eng. **138**, 041306 (2015).
[17] O. B. Usta, J. E. Butler, and A. J. C. Ladd, Phys. Fluids **18**, 031703 (2006).
[18] H. Haddadi and D. Di Carlo, J. Fluid Mech. **811**, 436 (2017).
[19] A. J. C. Ladd, J. Fluid Mech. **271**, 285 (1994).
[20] A. J. C. Ladd, J. Fluid Mech. **271**, 311 (1994).
[21] C. K. Aidun, Y. Lu, and E.-J. Ding, J. Fluid Mech. **373**, 287 (1998).
[22] B. Chun and A. J. C. Ladd, Phys. Rev. E **75**, 066705 (2007).
[23] M. Bouzidi, M. Firdaouss, and P. Lallemand, Phys. Fluids **13**, 3452 (2001).
[24] P. Lallemand and L. Luo, J. Comput. Phys. **184**, 406 (2003).
[25] D. d'Humières and I. Ginzburg, Phys. Rev. E **68**, 066614 (2003).
[26] P.-H. Kao and R.-J. Yang, J. Comput. Phys. **227**, 5671 (2008).
[27] J. Wu and C. K. Aidun, Int. J. Numer. Meth. Fluids **62**, 765 (2010).
[28] D. Goldstein, R. Handler, and L. Sirovich, J. Comput. Phys. **105**, 354 (1993).
[29] X. D. Niu, C. Shu, Y. T. Chew, and Y. Peng, Phys. Lett. A **354**, 173 (2006).
[30] C. S. Peskin, J. Comput. Phys. **25**, 220 (1977).
[31] C. Peng, O. M. Ayala, and L.-P. Wang, Comput. Fluids **192**, 104233 (2019).
[32] S. K. P. Sanjeevi, J. A. M. Kuipers, and J. T. Padding, Int. J. Multiphase Flow **106**, 325 (2018).
[33] R. Zhang, X. Shan, and H. Chen, Phys. Rev. E **74**, 046703 (2006).
[34] C. Coreixas, G. Wissocq, G. Puigt, J.-F. Boussuge, and P. Sagaut, Phys. Rev. E **96**, 033306 (2017).
[35] G. Pontrelli, A. Montessori, I. Halliday, M. Lauricella, S. V. Lishchuk, T. Spencer, and S. Succi, *Numerical Methods and Advanced Simulation in Biomechanics and Biological Processes* (Academic, New York, 2017).
[36] G. Di Staso, H. J. H. Clercx, S. Succi, and F. Toschi, J. Comput. Sci. **17**, 357 (2016).
[37] Z. Guo, B. Shi, T. Zhao, and C. Zheng, Phys. Rev. E **76**, 056704 (2007).
[38] E. H. T. Akenine-Möller, *Real-Time Rendering* (A K Peters, Natick, MA, 2002).
[39] E. Guazzelli, J. F. Morris, and S. Pic, *A Physical Introduction to Suspension Dynamics*, Cambridge Texts in Applied Mathematics (Cambridge University Press, Cambridge, 2011).
[40] H. B. J. Happel, *Low Reynolds Number Hydrodynamics*, Mechanics of Fluids and Transport Processes (Springer, Netherlands, 1983).
[41] T. Krüger, F. Varnik, and D. Raabe, Phys. Rev. E **79**, 046704 (2009).
[42] G. B. Jeffery and L. N. G. Filon, Proc. R. Soc. London Ser. A **102**, 161 (1922).
[43] M. S. Ingber and L. A. Mondy, J. Rheol. **38**, 1829 (1994).
[44] H. Huang, Y. Wu, and X. Lu, Phys. Rev. E **86**, 046305 (2012).
[45] J. Feng, H. H. Hu, and D. D. Joseph, J. Fluid Mech. **261**, 95 (1994).
[46] H. H. Hu, D. D. Joseph, and M. J. Crochet, Theor. Comput. Fluid. Dyn. **3**, 285 (1992).
[47] J. Feng, H. H. Hu, and D. D. Joseph, J. Fluid Mech. **277**, 271 (1994).
[48] H. Li, X. Lu, H. Fang, and Y. Qian, Phys. Rev. E **70**, 026701 (2004).
[49] B. Wen, C. Zhang, Y. Tu, C. Wang, and H. Fang, J. Comput. Phys. **266**, 161 (2014).
[50] C. K. Aidun and E-J. Ding, Phys. Fluids **15**, 1612 (2003).
[51] E-J. Ding and C. K. Aidun, J. Fluid Mech. **423**, 317 (2000).
[52] C. Zettner and M. Yoda, Exp. Fluids **30**, 346 (2001).